

THE COLD DUST CONTENT OF THE OXYGEN-RICH SUPERNOVA REMNANT G292.0+1.8

PARVIZ GHAVAMIAN¹, BRIAN J. WILLIAMS²

Draft version March 5, 2022

ABSTRACT

We present far-infrared images of the Galactic oxygen-rich supernova remnant (SNR) G292.0+1.8, acquired with the PACS and SPIRE instruments of the *Herschel Space Observatory*. We find that the SNR shell is detected in the PACS blue (100 μm) band, but not in the red (160 μm) band, broadly consistent with results from AKARI observations. There is no discernible emission from G292.0+1.8 in SPIRE imagery at 250, 350 and 500 μm . Comparing the 100 μm emission to that observed with *Spitzer* at 24 and 70 μm , we find a very similar appearance for G292.0+1.8 at all three wavelengths. The IR emission is dominated by dust from non-radiative circumstellar shocks. In addition, the radiatively shocked O-rich clump known as the 'Spur' on the eastern side of G292.0+1.8 is clearly detected in the PACS blue images, with marginal detection in the red. Fitting the existing 14-40 μm IRS spectra of the Spur together with photometric measurements from 70 μm MIPS and 100 μm PACS photometry, we place an upper limit of $\lesssim 0.04 M_{\odot}$ of ejecta dust mass in the Spur, under the most conservative assumption that the ejecta dust has a temperature of 15 K. Modeling the dust continuum in the IRS spectra at four positions around the rim, we estimate postshock densities ranging from $n_p = 3.5 \text{ cm}^{-3}$ to 11 cm^{-3} . The integrated spectrum of the entire SNR, dominated by swept up circumstellar dust, can be fit with a two-component dust model with a silicate component at 62 K and graphite component at 40 K for a total dust mass of $0.023 M_{\odot}$.

Subject headings: ISM: individual (G292.0+1.8), ISM: kinematics and dynamics, shock waves, plasmas, ISM: supernova remnants

1. INTRODUCTION

The Galactic supernova remnant (SNR) G292.0+1.8 was produced by an unrecorded SN that occurred roughly 3000 years ago (Ghavamian et al. 2005; Winkler & Long 2006; Winkler et al. 2009). It is classified as an oxygen-rich SNR based on the dominance of oxygen line emission in its optical spectrum. In [O III] $\lambda 5007 \text{ \AA}$ optical images G292.0+1.8 is dominated by a distinct, crescent-shaped structure approximately $1'$ in size (known as the 'Spur') located on the eastern side of the SNR (Goss et al. 1979). Modeling of spectra in the optical (Winkler & Long 2006) and mid-infrared (Lee et al. 2009; Ghavamian et al. 2009; Ghavamian et al. 2012) indicates a wide range of densities (~ 0.5 - 100 cm^{-3}) and shock velocities (~ 20 - 200 km s^{-1}) throughout the Spur. A collection of localized ejecta clumps (fast-moving knots, or FMKs) have also been found in the interior of G292.0+1.8 (Ghavamian et al. 2005; Winkler & Long 2006). This contrasts with the morphology of the SNR in X-ray (Clark et al. 1980; Park et al. 2002; 2004, 2007; Kamitsukasa et al. 2014; Bhalerao et al. 2015), radio (Gaensler & Wallace 2003) and infrared (Lee et al. 2009; Ghavamian et al. 2009, 2012) wavelengths, where the remnant appears as a slightly elliptical shell with maximum width of $8'$. The shell is approximately bisected by a belt of circumstellar material running E-W. The current consensus is that the shell is likely the relic of the progenitor star's equatorial winds (Park et al. 2002; 2004; 2007; Gonzalez & Safi-Harb

2004).

Here we report on far-infrared imaging observations of G292.0+1.8 obtained with the PACS and SPIRE instruments on the *Herschel Space Observatory*. The PACS images were taken in the 85-130 μm (blue, centered on 100 μm) and 130-210 μm (red, centered on 160 μm) bands. Emission at these wavelengths traces mostly the cool dust (~ 20 - 30 K) heated by shocks in the circumstellar medium (CSM). Our observations also included SPIRE imagery at 250, 350 and 500 μm , meant to probe the coldest dust ($\lesssim 20 \text{ K}$). The main results of our observations are the successful detection of cold dust in the radiatively shocked supernova ejecta of G292.0+1.8, as well as the successful detection of cold dust in the circumstellar shocks surrounding G292.0+1.8.

2. OBSERVATIONS AND DATA REDUCTION

The observations of G292.0+1.8 described in this paper were performed during OT2 of *Herschel* (PID 40583; P. Ghavamian, PI). They consisted of large scan maps of the SNR with the PACS instrument in imaging photometer mode on 2013 January 5, and included observations in blue (100 μm) and red (160 μm) channels. Additional observations of G292.0+1.8 were performed with the SPIRE instrument on 2012 June 23 at 250, 350 and 500 μm . The PACS observations used a medium speed map with 5 scan legs of length $10'$, with cross-scan steps separated by $110''$. The diameter of G292.0+1.8 is approximately $8.3'$ (14 pc at an assumed distance of 6 kpc; Gaensler & Wallace 2003), so the PACS scan map was constructed to allow sufficient coverage of the entire remnant and nearby background. The PACS scan map was repeated 80 times for a total exposure time (on-source) of 12,000 s. The $1\text{-}\sigma$ extended source sensitivity of the

¹ Department of Physics, Astronomy and Geosciences, Towson University, Towson, MD, 21252; pghavamian@towson.edu

² CRESST/USRA and X-ray Astrophysics Laboratory, NASA Goddard Space Flight Center, Greenbelt, MD, 20771; brian.j.williams@nasa.gov

PACS observations was approximately 1.8 MJy sr^{-1} at $100 \mu\text{m}$ and 1.1 MJy sr^{-1} at $160 \mu\text{m}$. The SPIRE images were acquired with a nominal speed scan map with $8'$ across and repeated 20 times for an on-source total exposure time of 1,649 s.

Our PACS data were processed with *Herschel* Interactive Processing Environment (HIPE) and converted to level 3 mosaics. The pixel scale of the mosaics was $1.6'' \text{ pixel}^{-1}$ in the blue channel and $3.2'' \text{ pixel}^{-1}$ in the red channel. The diffraction limited optics produce a full width at half maximum (FWHM) of $8''$ for the PACS PSF at $100 \mu\text{m}$ and $12''$, at $160 \mu\text{m}$. The flux calibration uncertainty for PACS is less than 10% (Poglitsch et al. 2010) and the expected color corrections for the PACS 100 and $160 \mu\text{m}$ channel are small compared to the calibration errors ($\lesssim 7\%$ for a blackbody with $20 \text{ K} \lesssim T \lesssim 50 \text{ K}$). We therefore adopt a 10% calibration error. The SPIRE data were also processed with HIPE and converted to level 2 products having pixel scale of $6'' \text{ pixel}^{-1}$, $10'' \text{ pixel}^{-1}$ and $14'' \text{ pixel}^{-1}$ at 250, 350 and $500 \mu\text{m}$, respectively. The corresponding PSF FWHM for the three SPIRE bands are $14''$ at $250 \mu\text{m}$, $25.2''$ at $350 \mu\text{m}$ and $26.6''$ at $500 \mu\text{m}$, respectively.

To enable comparison of photometry between the blue channel PACS image and the existing $70 \mu\text{m}$ *Spitzer* MIPS image of G292.0+1.8 (Ghavamian et al. 2012) we first used the IRAF task WREGISTER to transform the PACS $100 \mu\text{m}$ image to the same spatial scale and orientation as the MIPS $70 \mu\text{m}$ image. We then binned the transformed image to the same pixel scale as the latter, and finally convolved the binned image with the appropriate kernel to match the PSF of the MIPS $70 \mu\text{m}$ image. We used the IDL-based Convolution Kernels software CONVIMAGE (Gordon et al. 2008) with a kernel specifically designed to smear the PACS $100 \mu\text{m}$ PSF to that of the MIPS $70 \mu\text{m}$ PSF. To extract surface brightness values from G292.0+1.8 we utilized the FUNTOOLS package of SAO (<https://www.cfa.harvard.edu/~john/funtools/>).

As a supplement to our analysis in this paper, we have combined PACS photometric measurements from specific regions of interest around G292.0+1.8 with spectra extracted from the *Spitzer* IRS spectral imaging datacube (Ghavamian et al. 2012). The basic configuration used for those observations is described as follows. The IRS spectral observations consisted of mapping scans with both 1st and 2nd order Long-Low slits, which together covered the entire SNR in the $14\text{--}40 \mu\text{m}$ wavelength range. There were 560 individual spectra acquired, each at an exposure time of 32s pixel^{-1} . The analysis of that dataset is described in detail in Ghavamian et al. (2012), and the reader is referred to that paper for more information.

3. IMAGING RESULTS

The mosaicked level-3 images of G292.0+1.8 are shown side by side in Figure 1. The morphology of G292.0+1.8 at $100 \mu\text{m}$ is strikingly similar to its appearance in the MIPS $24 \mu\text{m}$ and $70 \mu\text{m}$ bands. An ellipsoidal shell, which coincides with the shell of emission seen in X-rays, can be seen at $100 \mu\text{m}$. The shell extends nearly three quarters of the way around G292.0+1.8, fading to invis-

ibility along the eastern quarter of the SNR. The lack of far IR emission on the eastern side of G292.0+1.8 is consistent with results from X-ray analyses, which indicate much lower preshock densities in that region than elsewhere along the rim (Lee et al. 2010). The equatorial belt, noted in previous X-ray (Park et al. 2004; Park et al. 2007, Lee et al. 2010) optical (Ghavamian et al. 2005) and infrared (Ghavamian et al. 2009; Lee et al. 2009; Ghavamian et al. 2012) observations can be seen stretching across the middle of G292.0+1.8 at $100 \mu\text{m}$. Detailed analysis of the shell at X-ray (Lee et al. 2010) and mid-infrared wavelengths (Ghavamian et al. 2012) showed an elevated preshock density along the southwestern edge of G292.0+1.8, consistent with features seen in the PACS $100 \mu\text{m}$ image. No portion of the shell or equatorial belt is detected at $160 \mu\text{m}$ (Figure 1). Emission clumps are seen both along the southwestern edge of G292.0+1.8 and immediately outside the shell. Although some of the clumpy emission knots along the southwestern edge of G292.0+1.8 at $100 \mu\text{m}$ are also present at $160 \mu\text{m}$, they have no X-ray or optical counterparts, thus indicating that their emission is not shock excited. They may be molecular cloud structures along the line of sight unrelated to G292.0+1.8. However, the elevated preshock density in this part of the SNR (Lee et al. 2010) may indicate some connection with G292.0+1.8.

No emission is detected from G292.0+1.8 in any of the three SPIRE bands (Figure 2). The clumpy emission knots seen outside the southwest corner of the remnant in the PACS images are also seen at 160, 250, 350 and $500 \mu\text{m}$, consistent with dense, cold clouds heated by ambient ultraviolet radiation. Again, the clumpy knots may be connected to a larger structure such as a molecular cloud along the line of sight.

No discernible emission is detected from unshocked ejecta dust in any of the *Herschel* images. This dust component is predicted to exist interior to the reverse shock remnants of core collapse explosions, and can be heated to temperatures $\sim 30\text{--}40 \text{ K}$ from photoionizing radiation emitted by the overlying shocked ejecta (Lee et al. 2015). Emission from cold unshocked ejecta dust was detected in *Herschel* PACS observations of Cassiopeia A (Barlow et al. 2010). However, in G292.0+1.8 emission from the cold ejecta dust falls below the PACS detection limit.

Finally, the radiative shocks in the Spur are clearly detected at $100 \mu\text{m}$ (Figure 1). The origin of this emission is discussed in Section 5. There is no obvious IR emission from the extensive X-ray emitting (shocked) ejecta.

4. COMPARISON TO OPTICAL AND X-RAY IMAGERY

Many of the shock-heated circumstellar structures observed in G292.0+1.8 at X-ray wavelengths are also detected in the PACS $100 \mu\text{m}$ band. The PACS $100 \mu\text{m}$ image is shown alongside a deep *Chandra* image (720 ks; Park et al. 2007) in Figure 3. X-ray spectral analyses of these structures (Park et al. 2004, 2007; Lee et al. 2010) found all of them to be of interstellar composition, an indication that their emission arises from shocked circumstellar gas. The features in common between the two bands are marked by arrows and numbered C1 through C9 in Figure 3 ('C' indicating 'circumstellar'). The outer shock wave (C1, C2, C5, C6, C10) is clearly detected in both the far IR and soft X-rays, as is the equatorial belt

(C8) and associated structures (C7, C9). The density of the equatorial belt ($n_H \sim 5 \text{ cm}^{-3}$, Park et al. 2004) is elevated relative to the outer blast wave shell ($n_H \sim 0.8\text{--}1.2 \text{ cm}^{-3}$; Lee et al. 2010), with correspondingly lower shock speeds in the belt ($\sim 500 \text{ km s}^{-1}$; Ghavamian et al. 2005) compared to the shell ($\sim 1500\text{--}2000 \text{ km s}^{-1}$; Lee et al. 2010). Under these conditions, shocks in the belt have begun to form recombination zones, consistent with the faint optical [O III] and H α emission detected from structures C7, C8 and C9 (Ghavamian et al. 2005). At least two compact knots of emission near the southwestern edge of G292.0+1.8 (C3, C4) are also detected in both bands. The *Chandra* spectra of these knots shows that they are of cosmic (sub solar) composition (Park 2010: private communication). It is unclear whether they are simply interstellar clouds, or whether they are part of the progenitor star’s wind. If the latter, then that would indicate a highly clumpy stellar wind structure.

None of the shocked ejecta seen at X-ray wavelengths exhibit any obvious counterpart in the PACS or SPIRE images, indicating that the dust within the X-ray ejecta is either too cold to emit significantly in those bands, or that it does emit in those bands but falls below the detection limit of *Herschel* in the allotted exposure time. The dust in the X-ray emitting ejecta is expected to be cold due to the low plasma density (Dwek, Foster & Vancura 1996; Borkowski et al. 2006; Williams et al. 2011). In Cassiopeia A, on the other hand, dust emission has been detected by *Spitzer* from the X-ray emitting ejecta (Smith et al. 2009). The difference is partly due to the fact that G292.0+1.8 is nearly 5 times older than Cassiopeia A, so that its ejecta have expanded to lower density than those of Cassiopeia A.

Although the Spur is detected at $100 \mu\text{m}$, none of the fainter optically emitting ejecta knots (such as the fast-moving knots, or FMKs) are detected. The difference is likely due to the higher density of the radiative shocks in the Spur compared to the FMKs, as found by Winkler & Long (2006) and Ghavamian et al. (2009). The higher gas density results in a higher temperature for the dust there, and hence greater emissivity in the PACS $100 \mu\text{m}$ band compared to the FMKs.

A magnified view of the region around the Spur (marked by the dotted square in Figure 3) is shown in Figure 4 in optical [O III] (Winkler et al. 2006), side by side with the PACS $100 \mu\text{m}$ and PACS $160 \mu\text{m}$ images. Radiatively shocked O-rich ejecta are labeled E1–E6 (‘E’ referring to ‘ejecta’). There is striking correlation between the brightest [O III] features at the top of the Spur (E1 and E2) and the corresponding features at $100 \mu\text{m}$. Faint emission from these features can also be discerned in the $160 \mu\text{m}$ image. Other, fainter [O III] clumps farther down the Spur (E3, E5 and E6) are clearly seen at $100 \mu\text{m}$, though not at $160 \mu\text{m}$ due to a combination of their faintness and lower spatial resolution at $160 \mu\text{m}$.

In addition to [O III] $\lambda 5007 \text{ \AA}$ emission, the oxygen-rich radiative shocks in the Spur can be expected to produce [O III] $88 \mu\text{m}$ emission. Most of the oxygen line emission is expected to arise from a region of nearly constant electron temperature ($\sim 10^5 \text{ K}$) behind the radiative shocks (Itoh 1981, 1988; Borkowski & Shull 1990). The one oxygen-rich SNR with a spectroscopically measured [O III] $88 \mu\text{m}$ flux is Cas A, where the

observed ratio, corrected for interstellar reddening toward Cas A ($A_V \approx 5$, Hurford & Fesen 1996), is $F_{[\text{O III}]}(88 \mu\text{m})/F_{[\text{O III}]}(5007 \text{ \AA}) \sim 0.1\text{--}0.14$ (Docenko & Sunyaev 2010). If we assume an intrinsically similar ratio for G292.0+1.8, then applying the appropriate interstellar reddening for G292.0+1.8 ($A_V \approx 2$, Winkler & Long 2006), the predicted ratio of $88 \mu\text{m}$ to 5007 \AA emission for G292.0+1.8 should only be ~ 0.02 (due to the lower impact of reddening on the 5007 \AA line in G292.0+1.8). Scaling this ratio now to the [O III] $\lambda 5007 \text{ \AA}$ surface brightness of clumps E1 and E2 in G292.0+1.8 (Winkler et al. 2006) results in a predicted [O III] $88 \mu\text{m}$ surface brightness that is at least an order of magnitude lower than observed in the PACS $100 \mu\text{m}$ image. Therefore, we do not expect a substantial contribution from [O III] $88 \mu\text{m}$ to the emission observed from the Spur at $100 \mu\text{m}$.

Finally, we considered the contribution of [O I] $63 \mu\text{m}$ emission to the $100 \mu\text{m}$ image. The observed ratio $F_{[\text{O I}]}(63 \mu\text{m})/F_{[\text{O III}]}(5007 \text{ \AA})$ after correction of interstellar reddening toward Cas A is approximately $0.07\text{--}0.1$ (Docenko et al. 2010), so again under the assumption that G292.0+1.8 exhibits a similar ratio, the [O I] $63 \mu\text{m}$ surface brightnesses of clumps E1 and E2 are predicted to be at least an order of magnitude lower than their observed surface brightnesses in the $100 \mu\text{m}$ image. Further reducing the likelihood of [O I] contamination is the transmission of the PACS channel at $63 \mu\text{m}$, which is only $\sim 0.5\%$ (Poglitsch et al. 2010). Therefore, we do not expect significant contribution from [O I] in the PACS $100 \mu\text{m}$ image either. Of course, we cannot for certain know the contributions of [O I] and [O III] lines to the far-infrared emission in the PACS image without a far infrared spectrum of the the ejecta. However, it appears reasonable to assume that the PACS blue band emission from the Spur arises from dust continuum within the ejecta, most likely formed during the SN explosion and now heated in the radiative shocks.

5. ANALYSIS

The background-subtracted photometric global fluxes from G292.0+1.8 at 24 , 70 and $100 \mu\text{m}$ are shown in Figure 6. The fluxes at 24 and $70 \mu\text{m}$ are taken from Ghavamian et al. (2012), while the PACS $100 \mu\text{m}$ flux is taken from the PACS image convolved to MIPS $70 \mu\text{m}$ resolution (see Table 2). An upper limit on the flux at $160 \mu\text{m}$ as measured from the PACS red channel is marked by the inverted triangle.

5.1. Dust Models of the Oxygen-Rich Ejecta in the Spur

The cold dust present in the oxygen-rich Spur is likely associated with radiatively shocked ejecta (Ghavamian et al. 2009, 2012), where the heating source of the dust would not be collisional heating by energetic particles, but radiative heating from the slow, radiative shocks. Physically modeling such emission is beyond the scope of this paper. However, we can still obtain useful information about the total mass and temperature of the radiating dust, useful for constraining how much dust can be formed in core-collapse supernovae.

We extracted the IRS spectrum from the Spur, along with the MIPS flux at $70 \mu\text{m}$ and the PACS fluxes at 100 and $160 \mu\text{m}$ (with the $160 \mu\text{m}$ data point being only an upper limit). Both the IRS spectral extraction and PACS

flux measurements were obtained from a rectangular region centered on the Spur, using a nearby background region located just outside the remnant. The SED of the Spur is shown in Figure 7 and the extracted fluxes are listed in Table 2.

We note that the spectra show a clear sign of silicate dust, the “shoulder” in the spectrum seen at $\sim 18 \mu\text{m}$. We therefore assumed a pure generic silicate dust, and fit with a two-temperature model. While it is true that a pure silicate grain model would not account for the possibility of a small amount of CSM dust projected along the line of sight to the Spur, even this dust would consist mostly of silicate grains (Weingartner & Draine 2001). As mentioned above, our aim is not to provide a detailed dust census, but to provide an upper limit on the total amount of dust present in the Spur. In this model we assumed a single grain size of $0.05 \mu\text{m}$, which is unphysical, but Temim & Dwek (2013) point out that such an assumption only serves to make the derived dust masses upper limits to the actual value, which again, is the parameter we seek for the Spur. We obtained the fit shown in Figure 7 with the combination of a hot component, with $T_{\text{hot}} = 114 \text{ K}$ and $M_{\text{hot}} = 5 \times 10^{-6} M_{\odot}$, and a cool component, with $T_{\text{cool}} = 52 \text{ K}$ and $M_{\text{cool}} = 1.2 \times 10^{-3} M_{\odot}$.

Finally, we estimated an upper limit on the dust mass under the most extreme assumption that a third, even colder, undetectable component were present. For this, we fixed the hot and cold components at their fitted values, but added a hypothetical dust component with an extreme temperature of $T = 15 \text{ K}$. We allowed the mass of this component to be as high as possible, without violating the measured upper limit on $160 \mu\text{m}$. Under this assumption, we found that the mass of this cold component was limited to $< 0.04 M_{\odot}$.

5.2. The Global Dust Spectrum

In the next part of our analysis, we considered the total amount of IR flux, integrated from the entire remnant. We constructed an SED using fluxes at 24, 70 from the estimate of Ghavamian et al. (2012), as well as the 100, and $160 \mu\text{m}$ estimates (shown in Figure 6). The emission line contribution is negligible, so that virtually all of the emission is produced by dust. As we showed above, this dust arises from different components (both ejecta dust and CSM dust), and even within the CSM dust, there are a variety of different physical conditions. It would be impossible to construct a unique physical model for all these different components, so we simply fit the SED in a similar fashion to that done for the ejecta dust in the Spur, with one modification: since the vast majority of the emission in the remnant is dominated by the bright CSM dust emission, we used a two-component model consisting of a silicate component and a graphite component, with the mass ratio between the two fixed at 2.5 (Weingartner & Draine 2001).

We find that the global spectrum of G292.0+1.8 can be fit well with a two-temperature dust model with $T_{\text{silicate}} = 60 \text{ K}$, $T_{\text{graphite}} = 39 \text{ K}$ (green and red dashed curves in Figure 6), with a total dust mass $M_{\text{dust}} = 0.023 M_{\odot}$. Again, this includes all sources of dust: CSM, equatorial belt, and supernova ejecta. By comparison, Lee et al. (2009) obtained similar results using a carbonaceous/silicate grain mix as prescribed by

Draine et al. (2003) and applying a two-temperature dust model to the AKARI global spectrum. They obtained a total dust mass of $4.5 \times 10^{-6} M_{\odot}$ for a warm component ($T = 103 \text{ K}$) and $\lesssim 0.048 M_{\odot}$ for a cold component ($T \sim 47 \text{ K}$).

The estimated mass of swept-up gas for G292.0+1.8 is $15\text{-}40 M_{\odot}$ (Lee et al. 2010), which combined with our dust mass estimate gives a dust to gas ratio of $(0.6\text{-}1.5) \times 10^{-3}$. This is significantly lower than the average dust-to-gas ratio of 6.2×10^{-3} (Zubko et al. 2004) for the interstellar medium, indicating a significant amount of dust destruction in the circumstellar shocks around G292.0+1.8. This is not unusual; for example, in a study of IR emission from Kepler’s SNR with *Spitzer*, Blair et al. (2007) found that 78% of the pre-existing CSM dust has been destroyed by the passage of the shock wave.

5.3. Dust in the Bright Circumstellar Ring

In the last part of our analysis we focused on modeling IRS spectra from four localized portions of the bright circumstellar ring (marked on Figure 5). These regions were chosen to sample the morphological variations observed in the *Spitzer* images. The shocks in these regions are some of the most clearly defined structures discernible in the IR. The regions include some of the faintest emission from the outer blast wave along the northern edge (Region 1), as well as circumstellar shocks with enhanced emission along the western rim (Regions 3 and 4). The emission in Region 2 is intermediate in surface brightness between the northern and western regions. In each case we subtracted a local background from a region of the same size, located immediately outside the remnant. One motivation for choosing localized regions, rather than a global average, was to take into account variability of the background emission around G292.0+1.8. As noted by Ghavamian et al. (2012), the background around G292.0+1.8 exhibits a positive surface brightness gradient running from E to W, correlated with the relatively higher surface brightness of the circumstellar shocks on the eastern side. We extracted IRS spectra for those regions from our IRS data cube and then subtracted an off-source background, as marked in Figure 5. The resulting background-subtracted IRS spectra are shown in Figure 8.

To model the dust spectra, we used a procedure identical to that in our previous work; see Borkowski et al. (2006) and Williams et al. (2012) for a full description. The heating of grains in the post-shock plasma by collisions with hot ions and electrons is modeled, taking grain size distributions for both silicate and graphite grains in the Milky Way in appropriate proportions (Weingartner & Draine 2001). The shock model calculates both the heating and subsequent destruction of grains due to sputtering, and predicts an output IR spectrum. The primary inputs are gas temperature, gas density, and ionization age of the plasma (defined as $\tau_p = \int_0^t n_p dt$, where n_p is the post-shock proton density). We fixed the electron temperature and ionization age in each region to those derived in Lee et al. (2010) (though note that the variations in these parameters have fairly small effect on the resulting dust spectrum). The proton temperature is assumed to be 5 keV for all regions, though this has an almost completely negligible effect on the fit (Williams et

al. 2011). The post-shock density, which has by far the largest effect, was then left as a free parameter to tune to obtain the best fit to the spectrum. We assumed cosmic abundances, so that the post-shock electron density is 20% higher than that of the protons.

The post-shock densities predicted by our fits are listed, with uncertainties, in Table 1, and the resulting fits to the IRS spectra are shown in Figure 8. The regions we selected for analysis differ from spatial regions examined by Lee et al. (2010); see Figure 4 of their paper. Our densities are a few times higher than those obtained by Lee et al. (2010) from the X-ray fits. However, this is to be expected since their regions sample the more rarefied emission of the outermost blast wave. Additionally, our regions likely are a superposition of emission from both components (i.e., circumstellar belt and more diffuse ambient medium just behind the blast wave shock). Given that G292.0+1.8 is believed to be expanding into an r^{-2} stellar wind, we would expect the densities interior to the blast wave emission to be higher. The densities we derive for the belt are quite similar to those derived for that structure by Park et al. (2007).

6. SUMMARY

We have presented PACS and SPIRE imaging observations of G292.0+1.8 obtained with *Herschel*. We have combined these observations with *Spitzer* datacube spectra (14-40 μm) to estimate the quantity of cold and warm dust in G292.0+1.8. We have taken advantage of the superior spatial resolution of *Herschel* PACS to identify regions of localized dust emission within the radiatively shocked O-rich ejecta in G292.0+1.8. This allows us to identify the presence of cold dust specifically associated with the O-rich radiative shocks.

Most of the cold dust in the remnant is morphologically associated with the prominent shell of circumstellar material identified in X-ray images. Thus, most of this dust is pre-existing, rather than newly-formed, and is being heated and destroyed by the forward shock into this

shell. We use the dust spectra from a few regions along the shell to derive the gas densities there, finding them to be $\sim 4 - 10 \text{ cm}^{-3}$, a few times higher than the densities of the emission from the elliptically shaped forward shock. This is consistent with the fact that the shell is substantially brighter in both X-rays and IR than the outermost material.

We find only a small amount of dust, about a thousandth of a solar mass, associated with the O-rich ejecta identified in optical images of the remnant. This may not account for all the ejecta dust present, but even if we consider *all* of the IR emission from the entire remnant, we obtain a total dust mass of only $0.023 M_{\odot}$.

G292.0+1.8 is only the third oxygen-rich supernova remnant, aside from 1E0102-72.3 (Sandstrom et al. 2009; Rho et al. 2009) and Cassiopeia A (Rho et al. 2008; Smith et al. 2009), having supernova ejecta dust detected at 100 μm with *Herschel*. Unlike the well known O-rich supernova remnant Cassiopeia A, where IR dust continuum has been detected by *Herschel* in all three components of the ejecta (radiative shocks, non-radiative (X-ray emitting) shocks and cold unshocked ejecta, Ennis et al. 2006; Smith et al. 2009), dust continuum from the ejecta in the much older SNR G292.0+1.8 is only detected from the densest radiative shocks in the Spur. This is consistent with the much greater age, and hence lower ejecta density of G292.0+1.8 compared to Cassiopeia A.

The authors wish to thank John Raymond for valuable discussions regarding the interpretation of the *Herschel* data, as well as the anonymous referee for patient reading of the manuscript and very helpful feedback. This work is based in part on observations made with *Herschel*, a European Space Agency Cornerstone Mission with significant participation by NASA. Support for this work, part of the NASA Herschel Science Center Theoretical Research/Laboratory Astrophysics Program, was provided by NASA through a contract issued by the Jet Propulsion Laboratory, California Institute of Technology under a contract with NASA.

REFERENCES

- Barlow, M. J., et al. 2010, *A&A*, 518, L138
 Bhalerao, J. Park, S., Dewey, D., Hughes, J. P., Mori, K. & Lee, J. 2015, *ApJ*, 800, 65
 Blair, W. P., et al. 2007, *ApJ*, 662, 998
 Borkowski, K. J. & Shull, J. M. 1990, *ApJ*, 348, 169
 Braun, R., Goss, W. M., Caswell, J. L., & Roger, R. S. 1986, *A&A*, 162, 259
 Borkowski, K. J., et al. 2006, *ApJ*, 642, L141
 Clark, D., Tuohy, I. & Becker, R. 1980, *MNRAS*, 193, 129
 Docenko, D. & Sunyaev, R. A. 2010, *A&A*, 509, A59
 Draine, B. T. 2003, *ARA&A*, 41, 241
 Dwek, E., Foster, S. M. & Vancura, O. 1995, *ApJ* 457, 244
 Ennis, J. A., Rudnick, L. Reach, W. T., Smith, J. D., Rho, J., DeLaney, T., Gomez, H. & Kozasa, T. 2006, *ApJ*, 652, 376
 Gaensler, B. M., & Wallace, B. J. 2003, *ApJ*, 594, 326
 Ghavamian, P., Hughes, J. P., & Williams, T. B. 2005, *ApJ*, 635, 365
 Ghavamian, P., Raymond, J. C., Blair, W. P., Long, K. S., Tappe, A., Park, S. & Winkler, P. F. 2009, *ApJ*, 696, 1307
 Ghavamian, P., Long, K. S., Blair, W. P., Park, S., Fesen, R. Gaensler, B. M., Hughes, J. P., Rho, J. P. & Winkler, P. F. 2012, *ApJ*, 750, 39
 Gonzalez, M., & Safi-Harb, S. 2003, *ApJ*, 583, L91
 Gordon, K., Engelbracht, C. W., Rieke, G. H., Misselt, K. A., Smith, J.-D. T. & Kennicutt, R. C. 2008, *ApJ*, 682, 336
 Goss, W. M., Shaver, P. A., Zealey, W. J., Murdin, P. & Clark, D. H. 1979, *MNRAS*, 188, 357
 Hurford, A. P. & Fesen, R. A. 1996, *ApJ*, 469, 246
 Itoh, H., *PASJ*, 1981, 33, 1 (1981)
 ———, *PASJ*, 1988, 40, 673
 Kamitsukasa, F., et al. 2014, *PASJ*, 66, 64
 Lee, H.-G., et al. 2009, *ApJ*, 706, 441
 Lee, J.-J., Park, S., Hughes, J. P., Slane, P. O., Gaensler, B. M., Ghavamian, P. & Burrows, D. N. 2010, *ApJ*, 711, 861
 Lee, Y.-H., Koo, B.-C., Moon, D.-S. & Lee, J.-J. 2015, *ApJ*, 808, 98
 Park, S., et al. 2002, *ApJ*, 564, L39
 Park, S., et al. 2004, *ApJ* 602, L33
 Park, S., et al. 2007, *ApJ* 670, L121
 Poglitsch, A., et al. 2010, *A&A*, 518, L2
 Rho, J. H., et al. 2008, *ApJ*, 673, 271
 Rho, J. H., Reach, W. T., Tappe, A., Hwang, U., Slavin, J. D., Kozasa, T. & Dunne, L. 2009, *ApJ*, 700, 579
 Sandstrom, K. M., Bolatto, A. D., Stanimirovic, S., van Loon, J. Th., & Smith, J. D. T. 2009, *ApJ*, 696, 2138
 Smith, J. D. T., Rudnick, L., DeLaney, T., Rho, J., Gomez, H., Kozasa, T., Reach, W., Isensee, K. 2009, *ApJ*, 693, 713
 Temim, T., & Dwek, E. 2013, *ApJ*, 774, 8
 Vancura, O., Raymond, J. C., Dwek, E., Blair, W. P., Long, K. S. & Foster, S. 1994, *ApJ*, 431, 188
 Weingartner, J.C. & Draine, B.T. 2001, *ApJ*, 548, 296
 Williams, B. J. et al. 2011, *ApJ*, 729, 65
 Williams, B. J., et al. 2012, *ApJ*, 755, 3

Winkler, P. F., & Long, K. S. 2006, AJ, 132, 360

Winkler, P. F., Twelker, K., Reith, C. N. & Long, K. S. 2009, ApJ,
692, 1489

Zubko, V., Dwek, E. & Arendt, R. G. 2004, ApJS, 152, 211

TABLE 1
DERIVED DENSITIES FROM
MODELING OF IRS
SPECTRA

Region	n_p (cm^{-3})
1	$3.5^{3.9}_{3.2}$
2	$4.2^{4.5}_{3.9}$
3	$11.0^{11.3}_{10.6}$
4	$10.3^{10.5}_{10.1}$

NOTE. — Post-shock proton densities for the four spectra fit in Figure 8. Uncertainties are 90% confidence limits from χ^2 fits to IRS spectra.

TABLE 2
FLUXES UTILIZED IN MODEL FITS IN FIGURES 6 AND 8

Region	F(24) (Jy)	F(70) (Jy)	F(100) (Jy)	F(160) (Jy)
Global SED	9.8 ± 0.98^a	26.4 ± 4.2^a	20.2 ± 3.0	≤ 8.5
Spur	\dots^b	\dots^b	1.26 ± 0.2	0.57 ± 0.07

NOTE. — a) Fluxes as reported in Ghavamian et al. (2012). b) Models are fit to IRS spectra at these wavelengths

“““

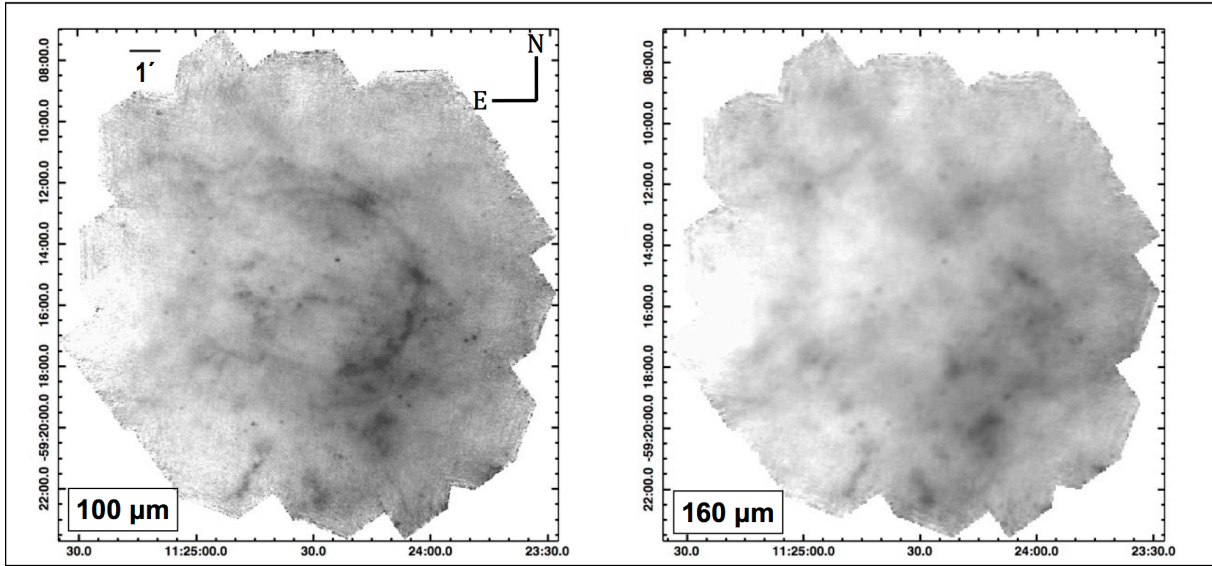


FIG. 1.— PACS blue band (left) and red band (right) images of G292.0+1.8. The outer shock can be seen on the western side as a partially complete elliptical shell on the western edge of the SNR.

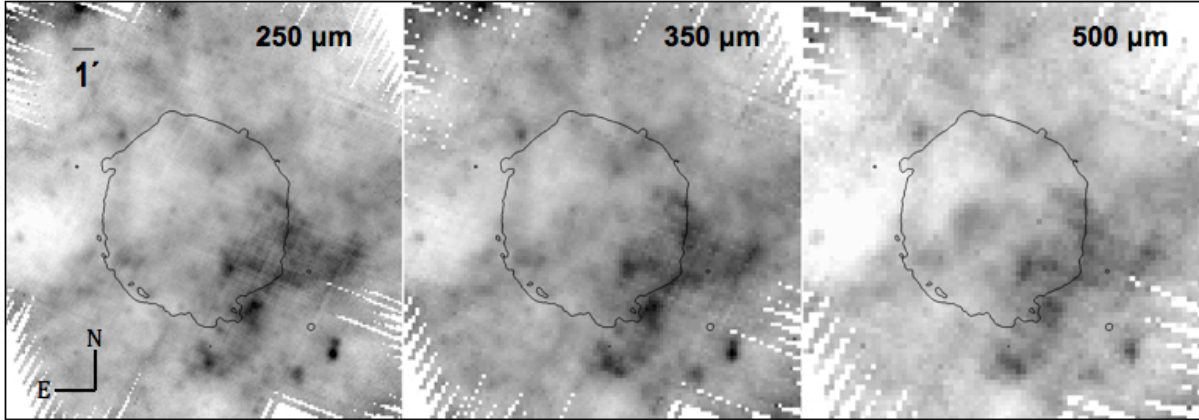


FIG. 2.— SPIRE images of G292.0+1.8, shown at 250, 350 and 500 μm with the outermost soft X-ray contour (0.3-1.0 keV; Park et al. 2007) marked. The images are dominated by unrelated background/foreground emission, with no discernible contribution from the SNR.

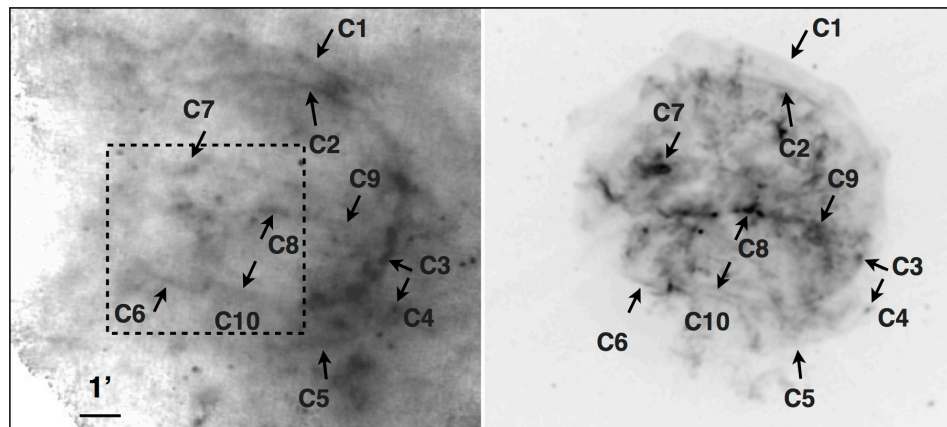


FIG. 3.— Comparison of the $100\ \mu\text{m}$ PACS and the deep X-ray *Chandra* images (Park et al. 2007) of G292.0+1.8. Prominent features discernible in both bands are marked C1-C10. The dashed square indicates the region used for the closeup of the oxygen-rich Spur in Figure 4.

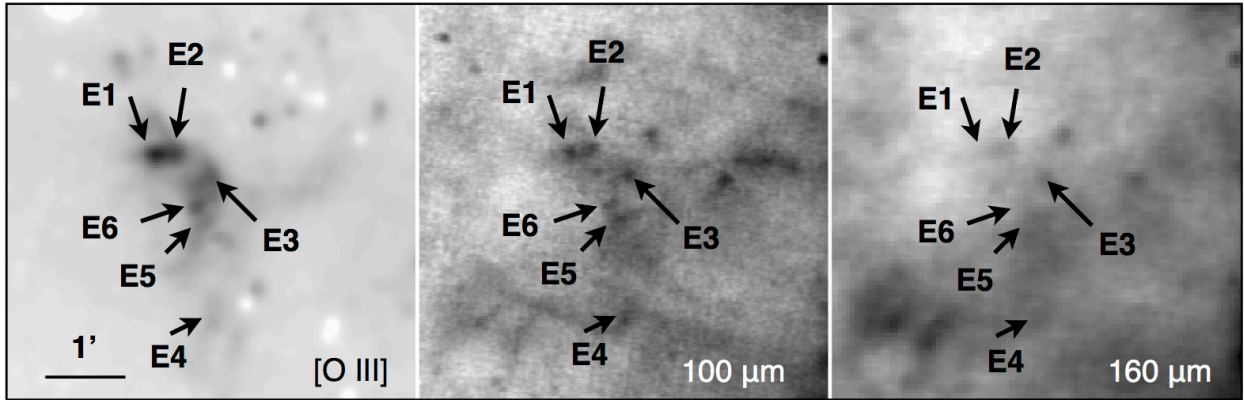


FIG. 4.— Closeup of the Spur, a dense clump of radiatively shocked ejecta, shown in [O III] (left; Winkler et al. 2006), at 100 μm (center) and 160 μm (right). Most of the Spur is discernible at 100 μm . Prominent features discernible in both [O III] and 100 μm are marked E1-E6.

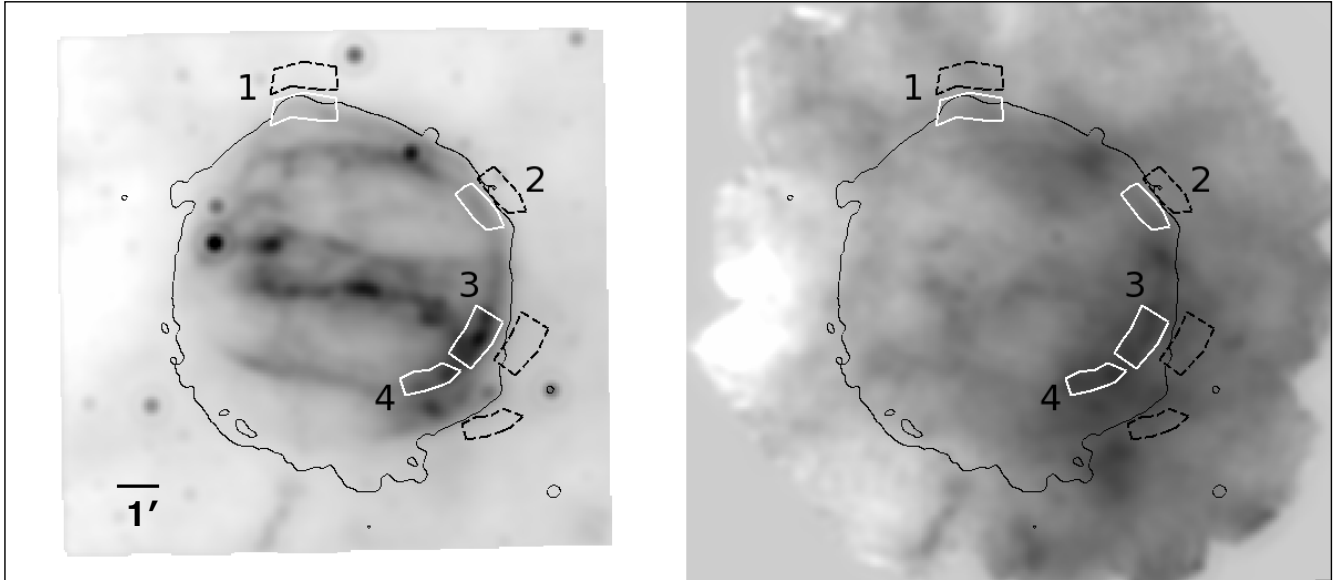


FIG. 5.— Left: *Spitzer* MIPS Image of G292.0+1.8 at $24\ \mu\text{m}$ (Ghavamian et al. 2012). Right: The *Herschel* PACS $100\ \mu\text{m}$ image of G292.0+1.8. The black contour marks the outer edge of the supernova remnant as measured from the *Chandra* X-ray image of the SNR (Park et al. 2007). The spatial resolution and pixel scales of both images shown here have been coarsened to that of the $70\ \mu\text{m}$ MIPS band of *Spitzer* (see text for details). The integrated fluxes from G292.0+1.8 at $24\ \mu\text{m}$ and $100\ \mu\text{m}$ reported in Figure 6 were obtained from these images. Regions used for extracting the IRS spectra in Figure 8 are marked with the white regions, and the corresponding backgrounds are marked with dotted black regions.

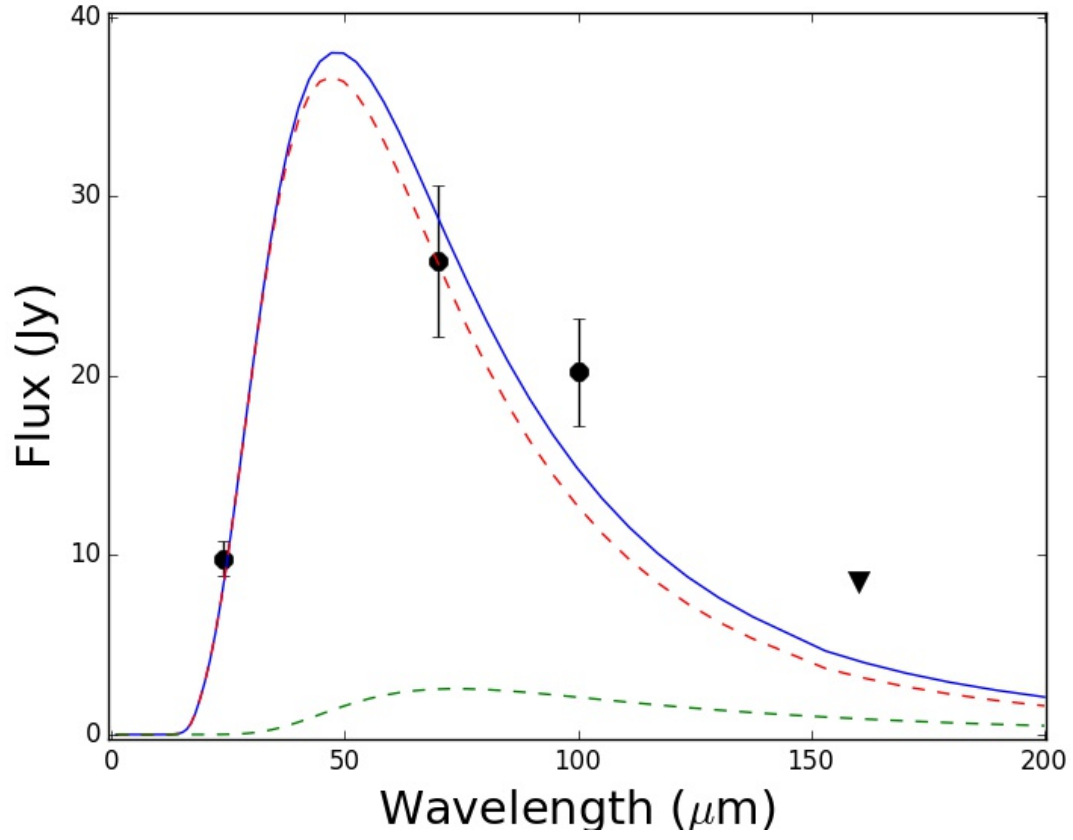


FIG. 6.— Global infrared SED of G292.0+1.8, with data points taken from the MIPS 24 μm and 70 μm images (Ghavamian et al. 2012) as well as the PACS 100 μm image and PACS 160 μm image (the latter is an upper limit, as no obvious emission is detected from G292.0+1.8 at 160 μm). A best-fit model to the 24, 70 and 100 μm data points is indicated with the blue line, with individual components of silicate grains indicated with the red dashed line and graphite grains indicated with the green dashed line (see text for details).

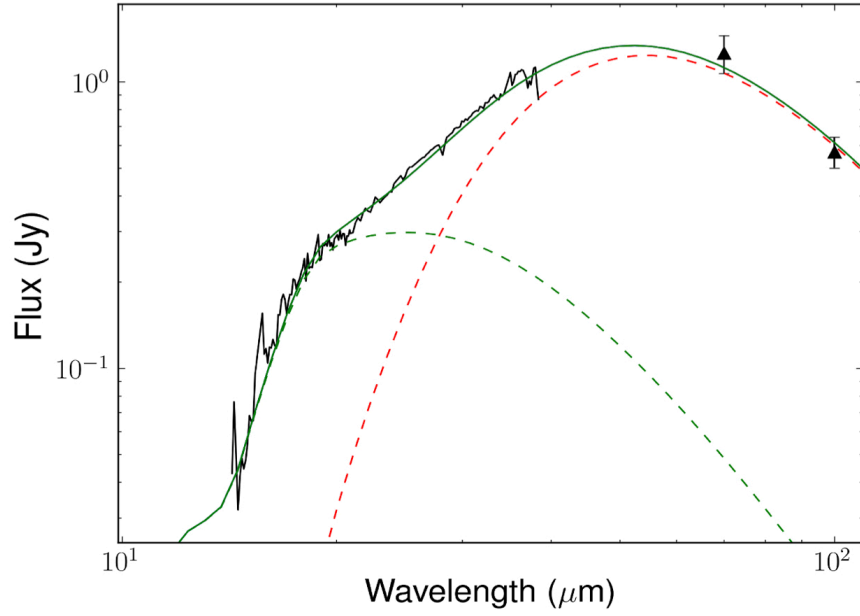


FIG. 7.— Integrated spectrum of the radiatively shocked O-rich Spur. The 15-40 μm component was obtained from the *Spitzer* IRS spectral map of G292.0+1.8 (Ghavamian et al. 2012), while the data points at 70 μm and 100 μm are from *Spitzer* MIPS and Herschel PACS, respectively. The spectrum reflects contributions from both shocked circumstellar dust and ejecta dust, due to line of sight superposition of the two components. The spectrum is fit with a hot component (green dotted line) and cool component (red dotted line).

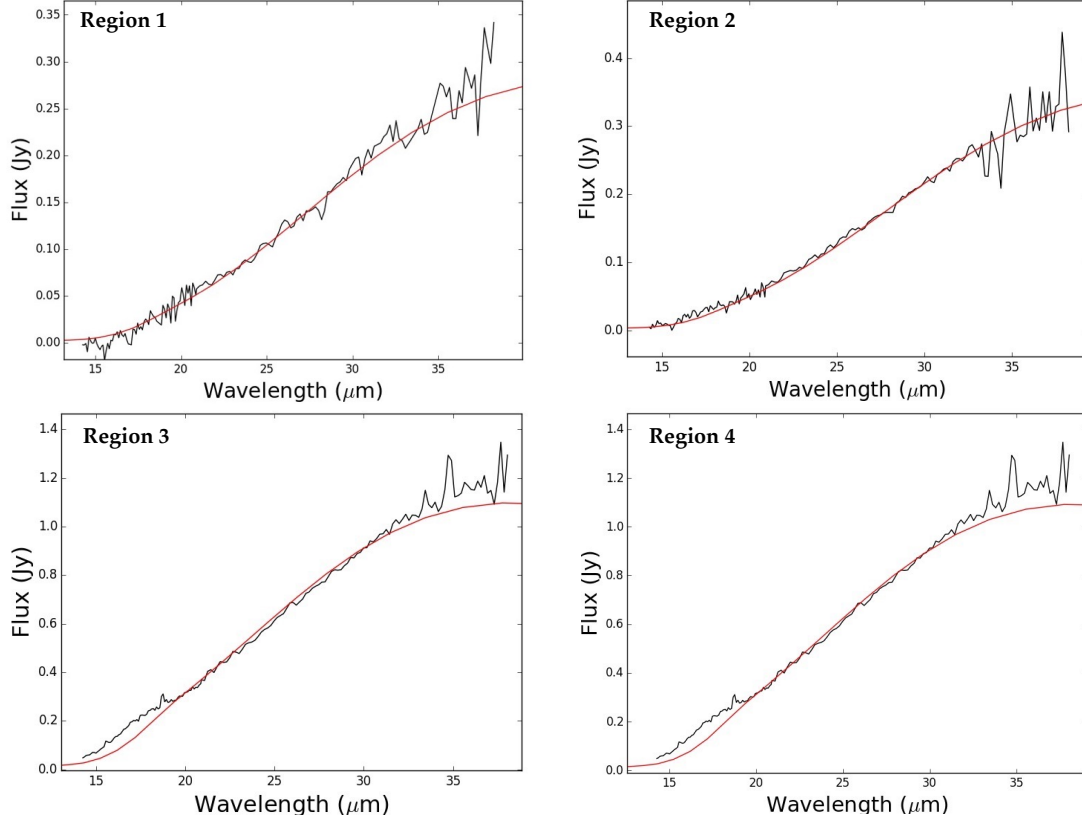


FIG. 8.— Background-subtracted *Spitzer* IRS spectra of four locations around the rim of G292.0+1.8 (regions marked in Figure 5). Shock model fits to each spectrum are marked with red lines.